Task-Based Control and Design of a BLDC Actuator for Robotics

Avik De*†, Abriana Stewart-Height*, and Daniel E. Koditschek*

***Abstract*—This paper proposes a new multi-input brushless DC motor current control policy aimed at robotics applications. The controller achieves empirical improvements in steady-state torque and power-production abilities relative to conventional controllers, while retaining similarly good torque-tracking and stability characteristics. Simulations show that non-conventional motor design optimizations whose feasibility is established by scaling model extrapolations from existing motor catalogues can vastly amplify the effectiveness of this new control-strategy.**

***Index Terms*—Force Control, Motion Control**

I. Introduction

A. Motivation and Background

As information processing technology becomes ever cheaper, smaller and more capable, motivation grows for using higher capacity sensing and computing to increase the mass specific work output of robot actuators. In this paper, we explore the benefits of bringing multi-input current control methods to bear on brushless DC (BLDC) servomotors for enhanced robotics applications. BLDC motors have remained the most effective electromagnetic actuation technology in robotics for applications that require high mass-specific power, despite the continued prevalence of hydraulic, pneumatic, and other technologies [1]. Robotic actuators are traditionally modeled as a torque source [2], and consequently a single BLDC actuator is typically abstracted as a single-input (commanded torque), single-output (produced torque) "torque amplifier" (TA). While the TA abstraction reduces model complexity, it also implicitly constrains the actuator's inner control algorithms to high-gain output-torque-tracking. This has the following implications for their control and design:

First, in terms of performance, the TA abstraction confines not just the peak speed, but as we discuss in this paper, also the peak torque and mechanical power output in a (typical) voltage-constrained scenario. Second, past studies on the design of robotic actuators [1], [3]–[5] have focused primarily on continuous and peak torque production per unit mass, while remaining within the confines of the TA paradigm.

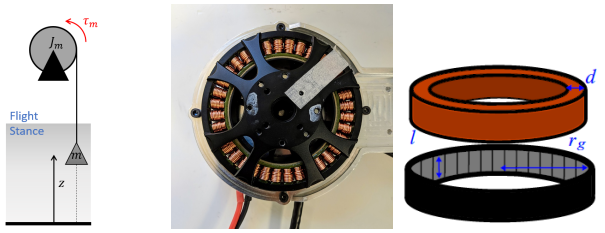

Figure 1: **Left:** Braking and 1DOF inverted hopping experiment setup (Sec. IV); **middle:** A T-motor U8 motor [10] with a Ghost Robotics reprogrammable motor controller [11] used for the experiments; **right:** Stator and rotor of a motor showing the critical geometric constants which are related to its performance (shown using our models in Sec. V). This figure is reproduced from [5].

On the other hand, almost a century of motor and power electronics literature has thoroughly analyzed aspects of control and design of a BLDC actuator. Due to their ubiquity in legged robotics [3], [4], [6] and analytical tractability [7], we limit our scope to radial-flux, three-phase, brushless permanent-magnet synchronous motor with a non-salient rotor, following the taxonomy of [8] (though we simply refer to this class as "BLDC" here). In addition, we assume that the magnets produce an airgap flux density that is a sinusoidal function of the rotor angle [8, Fig. 2.20]—a standard assumption made in the motor literature when analytical conclusions are desired [7]. We also adopt the standard vector control—or field-oriented control (FOC)—method, which typically implements current regulation in the synchronous (with the rotor angle) frame. The motor literature discusses operation of BLDC motors far from the TA abstraction: "field angle control" can be used to control terminal power factor, optimize copper loss, control torque in a salient machine, or implement flux-weakening [8], [9]. However, in each of these cases, the motor is used in a very narrow operating regime and it is not clear how to bridge the gap between the needs of a general-purpose robotic actuator and the task-specification for the motor control algorithm. In this paper, we limit our scope to actuator usage as a torque source only (excluding, for example, field-weakening), in settings where the TA abstraction is used.

Returning to robotics, the relevant literature is more focused on aspects of motor selection than of control. After initial foundational work motivated by the design of robotic manipulators [1], [12], [13], recent research has focused on the demands of even more power-dense applications such as legged robotics [3], [4], [14] (also the application domain that motivates the tasks selected in Sec. IV).

Manuscript received: September 10, 2018; Revised December 5, 2018; Accepted January 5, 2019.

This paper was recommended for publication by Editor Paolo Rocco upon evaluation of the Associate Editor and Reviewers' comments. This work was supported in part by AFRL grant #FA865015D1845 subcontract 669737-1, and in part by ONR grant #N00014-16-1-2817, a Vannevar Bush Fellowship held by the last author, sponsored by the Basic Research Office of the Assistant Secretary of Defense for Research and Engineering.

*Electrical and Systems Engineering, University of Pennsylvania, Philadelphia, PA, USA. {avik,abrianas,kod}@seas.upenn.edu.

†Ghost Robotics Corp., Philadelphia, PA, USA. The first author is an officer and engineer at Ghost Robotics, but does not receive any compensation from the use of their products. The authors do not expect that publication of this paper would affect the commercial standing of the company in any way.

Digital Object Identifier (DOI): see top of this page.

Table I: Table of important symbols

Symbol	Brief description	Symbol	Brief description
TC	Torque control (7)	VC	Voltage control (8)
AC	Angle control (10)	CF	Current feedback
$v \in \mathbb{R}^3$	Phase voltages	$\imath \in \mathbb{R}^3$	Phase currents
$n \in \mathbb{Z}_+$	# pole pairs	$\theta_e \in S^1$	rotor elec. angle
$\omega_m = n\dot{\theta}_e$	mech. speed	$J_m \in \mathbb{R}$	rotor inertia
$\tau_{\text{ext}} \in \mathbb{R}$	external torque	R	resistance
L	inductance	k_e	linkage flux
$\beta(\theta_e)$	back-EMF waveform	$x \in \mathbb{R}^2$	rotor frame currents
$u \in \mathbb{R}^2$	rotor frame voltage	S	skew matrix $\left[\begin{smallmatrix} 0 & 1 \\ -1 & 0 \end{smallmatrix}\right]$
$\tau_e = \frac{nL}{R}$	elec. time constant	$r(\omega_m)$	$(1, \omega_m \tau_e)$
r_g	air-gap radius	d	stator depth
l	annular stat. thickness	n_t	turns per tooth
m	motor mass	l_w	wire length
v_w	wire volume	B	mag. field strength
K_m	motor const. $\frac{Nm}{\sqrt{W}}$		

For these selection and design studies, there are two popular approaches in the literature: (simple-)model-based selection (e.g. [1], [15]), and finite-element modeling (e.g. [16]). The deficiency of the first approach is that the typical scalar model of a TA-abstracted actuator is a strict restriction[1] of the dynamics of a BLDC actuator, and thus hides many aspects of its dynamic capabilities and constraints. On the other hand, finite element models are computationally expensive and hard to generalize. We follow the approach of [3], [4] and develop a predictive scaling model which correlates motor performance with a handful of parameters used in its construction.

B. Claims and Organization

The advent of sensor-abundant and computationally capable microcontrollers encourages a reconsideration of the traditional TA abstraction with the prospect of "opening up" the BLDC actuator and coupling its internal control algorithm to the varying needs of the task at hand. We propose a new control strategy that discards the TA abstraction, and in implementation on a physical one degree of freedom robot actuator (Fig. 1) empirically exhibits improvements in the steady-state torque- and power-production abilities (Sec. III-A) while retaining good torque-tracking and stability characteristics (Sec. III-B). Using analysis and numerical simulations, we show that non-conventional motor design optimizations can vastly amplify the effectiveness of this new control-strategy (Sec. III-C). Finally, we argue that such motor designs are feasible using a scaling-model-based extrapolation of motor catalog data (Sec. V).

Sec. II introduces a model for BLDC motors that forms the basis of our results. We also present two conventional control strategies used in robotic actuators in order to have a baseline for comparing new control strategies. Sec. III introduces a new controller (10) designed to maximize steady-state torque output by recruiting not just the q-axis current, but also the d-axis current for this purpose. We describe its implications for thermal as well as mechanical steady-state and transient performance, and also show how motor design interacts with the performance benefits offered by this new control strategy. Sec. IV introduces some (appropriately restricted versions of) tasks motivated by robotic applications—braking and hopping—and shows the effectiveness of the new control strategy in this real-world setting. Sec. V shows that a hypothetical new motor design that amplifies the benefits of the new controller is feasible, based on a scaling model of motor characteristics that we validate on motor catalog data. Sec. VI concludes and motivates future work in this area.

[1] as we observe at the end of Sec. II-A

II. Background on BLDC Motors

A. Modeling

With the notation in Table I, for a nonsalient[2] rotor, we have the motor equations [17]

$$\begin{aligned} L\dot{\imath} &= v - R\imath - k_e \omega_m \beta(\theta_e) \\ J_m \dot{\omega}_m &= k_e \beta(\theta_e)^T \imath + \tau_{\text{ext}}, \end{aligned} \tag{1}$$

where the design parameters are listed in Table I and

$$\beta(\theta_e) := \big(\sin(\theta_e), \sin(\theta_e + 2\pi/3), \sin(\theta_e + 4\pi/3)\big) \tag{2}$$

is the assumed-sinusoidal back-EMF waveform. We change coordinates to the rotor ("d-q," or "direct-quadrature") frame for both the states and inputs,

$$x = \begin{bmatrix} \beta & \beta_\perp \end{bmatrix}^T \imath =: E\imath, \qquad u := Ev. \tag{3}$$

For implementation purposes, we assume that θ_e is known accurately and without any (modeled) lag. Applying this coordinate change to (1), we get

$$\begin{aligned} \dot{x} &= E\dot{\imath} + \dot{E}\imath = Ei + SE\dot{\theta}_e L \\ &= Ei + \omega_m n SE\imath = \tfrac{1}{L} E(v - \imath R - k_e \omega_m \beta) + n\omega_m S x. \end{aligned}$$

Putting it all together,

$$\begin{aligned} \dot{x} &= A(\omega_m)x + u/L - k_e \omega_m e_1 / L \\ J_m \dot{\omega}_m &= k_e x_q + \tau_{\text{ext}}, \end{aligned} \tag{4}$$

where $A(\omega_m) = -\frac{R}{L} I_2 + n\omega_m S$. Lastly, with $\tau_e = nL/R$ the electrical time constant [3], consider the vector r (Table I) that intuitively captures the speed-dependent coupling between the q, d axes. We can reparameterize $A(\omega_m) = n(-\frac{1}{\tau_e} I_2 + \omega_m S)$, and also that $r(\omega_m) = -\frac{\tau_e}{n} A(\omega_m) e_1$, a scaled version of the first column of $A(\omega_m)$.

We observe here that the first row of the rotor-frame BLDC model (4) with the direct-axis current $x_d \equiv 0$, recovers $L\dot{x}_q = -Rx_q + u_q - k_e\omega$, which is identical to the scalar motor model used in a large amount of literature (e.g. [1]).

Additionally, note that magnitude of the control input is constrained to $\|u\| \le V_{\text{lim}}$ the available[4] voltage, typically implemented with a normalization step just before commands are sent to the drive electronics,

$$\text{constrain}(u) := V_{\text{lim}} \,\text{clip}(\|u\|) \tfrac{u}{\|u\|}, \tag{5}$$

where $\text{clip} : \mathbb{R} \to [0, 1]$ constrains a scalar to $[0, 1]$.

[2] As shown in [8, Figure 5.15], the rotor types in a BLDC actuator are (a) nonsalient (surface magnet, $L_d = L_q$), or (b), (c) salient (interior magnet, $L_d \neq L_q$). Here we set $L_d = L_q =: L$.

[3] multiplied by the number of pole pairs to account for the fact that we have chosen to work with the coordinate ω_m, the mechanical, not electrical, rotor velocity

[4] Here V_{lim} is assumed to be the upper bound on the dq-frame voltage u. Depending on implementation considerations such as maximum allowed PWM duty cycle, and the scaling of the inverse Clarke transform to move u back to the stator frame, $V_{\text{lim}} < V_{\text{bus}}$ the bus voltage.

B. Conventional Control Approaches

The TA abstraction is of a single-input torque source, despite u being 2-dimensional in (4). In this paradigm, x_q^* is the commanded q-axis current, and $x_d^* \equiv 0$. The latter is often fixed since a simple energy balance shows that

$$\begin{aligned} x^T\dot{x} &\overset{(4)}{=} x^T(-R/Lx + n\omega_m Sx) + x^T u/L - k_e\omega_m x_1/L \\ &= -R/Lx^T x + x^T u/L - \tau_m\omega_m/L; \end{aligned}$$

rearranging which we see that in any equilibrium condition,

$$x^T u = Rx^T x + \tau_m\omega_m. \tag{6}$$

The terms above show how the input electrical power $x^T u$ balances with wasteful Joule heating $Rx^T x$ and output mechanical power $\tau_m\omega_m$. Thus, Rx_d^2 naively contributes to wasteful heat, but not to output work in steady-state operation. Nonetheless, we show in various examples in III-A how x_d can be beneficial to tasks.

In the remainder of this subsection we present two conventional approaches to controlling (4), in order to have a baseline for comparison in the next sections. As expected from the dynamics (4), the availability of current feedback (CF) unlocks superior performance for all control strategies at the cost of hardware complexity and sensor noise (which we discuss in Sec. III-A3).

1) Feedback torque control (TC): In our notation, field-oriented control is conventionally [18] implemented in the rotor frame (4) with PI current control and (optionally) feedforward decoupling by canceling the natural dynamics. Given a desired current, x^*, let e_I be the integrated current error, such that $\dot{e}_I = x - x^*$. The controller then is

$$u_{\text{TC}} = -k_P(x - x^*) - k_I e_I + k_e\omega_m e_1 - LA(\omega_m)x. \tag{7}$$

In addition, the usual level of abstraction of "torque control" sets $x_d^* \equiv 0$.

We observe that this strategy requires exact knowledge of armature electrical parameters (R, L, k_e) as well as high-fidelity measurements[5] of θ_e, ι, and optionally ω_m for feedforward compensation.

2) Voltage control (VC): This position-based open loop strategy (e.g. [19], [20]) is the least susceptible to sensor noise since the only measurement required is the rotor angle θ_e to effect the coordinate transformation (3). Set

$$u_{\text{VC}} = \begin{cases} (Rx_q^*, 0) & \text{CF unavailable,} \\ (k_P(x_q^* - x_q), 0) & \text{using CF.} \end{cases} \tag{8}$$

The closed loop dynamics are

$$\begin{aligned} \dot{x}_q &= -R/L(x_q - x_q^*) + \omega_m(nx_d - k_e) \\ \dot{x}_d &= -R/Lx_d - \omega_m n x_q \end{aligned}$$

[5]Though the diagonal $-R/L$ terms in A are instrinsically stabilizing, the convergence rate is limited to the electrical time constant of the motor. Additional feedback through k_P, k_I is often used for faster convergence rates (especially in the presence of changing x^* commands). We investigate stability issues more in Sec. III-B.

Observe that when $\omega_m \to 0$ the closed loop system converges to $(x_q^*, 0)$, making this strategy usable[6] in low-speed (ω_m small) or low-inductance (L small) applications.

We further investigate the closed loop equilibria and stability properties of these controllers in III-B.

III. Task-based dq BLDC motor control

We introduce a task-specific new control strategy in this paper (whose goal is to maximize equilibrium torque production) and describe its utility in robotic applications in the next few sections. Note from the structure of A that

$$A(\omega_m)^{-1} = \left(\tfrac{L}{R\|r(\omega_m)\|}\right)^2 A(\omega_m)^T = \tfrac{-L}{R\|r\|^2}\begin{bmatrix} r^T \\ r_\perp^T \end{bmatrix}. \tag{9}$$

We suggest a new controller that abandons the TA abstraction, and uses both d, q-axes of control to align with r,

$$u_{\text{AC}} := \frac{\upsilon r(\omega_m)}{\|r(\omega_m)\|}, \text{ where} \tag{10}$$
$$\upsilon := \begin{cases} Rx_q^* & \text{CF unavailable,} \\ k_P(x_q^* - x_q) & \text{using CF,} \end{cases}$$

i.e. the magnitude scaling term is chosen differently depending upon whether current feedback is available or not. Note that we have defined $r(\omega_m)$ (Table I) such that it only depends on a single scalar design parameter, τ_e, and a single sensor measurement, ω_m, making the "no current feedback" version particularly insensitive to parameter/state uncertainty.

Reinterpreting $\angle r(\omega_m)$ as the "lead angle" or "phase-advance angle," this controller is related to sensorless BLDC control techniques that aim to keep the back EMF waveform $\beta(\theta_e(t))$ and the current waveform $\iota(t)$ in phase [21]. However, in addition to the benefits of these methods, the state-feedback controller (10) can be utilized in non-steady tasks such as those in Sec. IV, and also can be combined with current feedback seamlessly.

In III-A–III-B we investigate performance implications relative to the conventional strategies of II-B with a specific motor design (U8), and in III-C we investigate how design parameters of the motor can drastically amplify the benefits of dq control, motivating Sec. V.

A. Steady-State Operation

We first evaluate different performance measures at equilibria of (4) with various control strategies, including the conventional ones of II-B, compared to a task-specific controller that utilizes both available inputs in u. In this subsection, we denote the equilibrium states and inputs with a $\bar{\cdot}$ decoration.

From (4), at an equilibrium $\dot{x} = 0, x = \bar{x}, \omega_m = \bar{\omega}_m$, and

$$\bar{u} = k_e\bar{\omega}_m e_1 - LA(\bar{\omega}_m)\bar{x} = k_e\bar{\omega}_m e_1 + R[r, r_\perp]\bar{x}, \tag{11}$$

and using (9),

$$\bar{x} = \tfrac{-A(\bar{\omega}_m)^{-1}}{L}(\bar{u} - k_e\bar{\omega}_m e_1) = \tfrac{(\bar{u} - k_e\bar{\omega}_m e_1)}{R\|r\|^2}\begin{bmatrix} r^T \\ r_\perp^T \end{bmatrix}, \tag{12}$$

and the equilibrium q-axis current is the first row

$$\bar{x}_q = \tfrac{1}{R\|r\|^2}(r^T\bar{u} - k_e\bar{\omega}_m). \tag{13}$$

[6]However, note, as we show in Fig. (6), the attained equilibrium can get quite far away from the desired one at higher speeds.

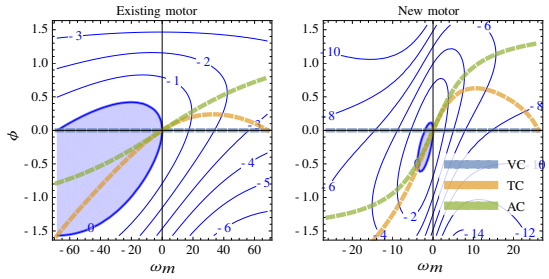

Figure 2: *Peak torque* $k_e(x_q - V_{\text{lim}}/R)$ *in Nm:* These plots show in blue τ_m-contours at different equilibrium states $\bar{\omega}, \bar{\phi} := \angle \bar{u}$ (11). The lines show the $\bar{\phi}$ selected by the 3 controllers (8), (7), (10) when directed to maximize x_q. The hypothetical new motor's parameters are shown in Fig. 7. From (13) and (10), the AC strategy is guaranteed to produce the highest $\bar{\tau}_m$. The significance of the shaded region, as in Fig. 3, is described in Sec. III-A1.

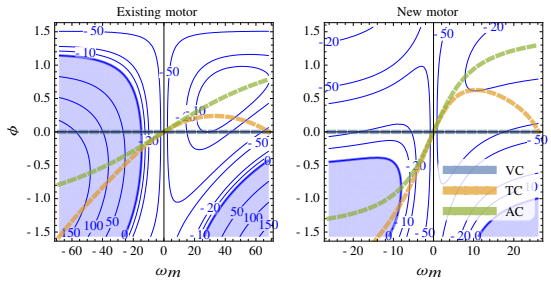

Figure 3: *Peak power* $|\tau_m \omega_m| - V_{\text{lim}}^2/(4R)$ *in W:* These plots show in blue contours of equilibrium power output, showing (as in Fig. 2) that the AC strategy exactly follows the gradient of maximum power. The shaded region is as in Fig. 2.

1) Peak torque: We consider a task where for each $\bar{\omega}_m$, the goal is to maximize (subject to fixed terminal voltage)[7] $\tau_m = k_e \bar{x}_q$. From the structure of (13), it is intuitively clear that (10) maximizes $\bar{x}_q$.

For peak torque, the VC strategy applies the maximum allowed voltage to the q-axis $u_{\text{VC}} \equiv (V_{\text{lim}}, 0)$, but the TC strategy still attempts to control x_d to 0. For this equilibrium analysis, we first use (11) with $\bar{x}_d \equiv 0$ to find the requisite $\bar{u}$ vector to keep $x_d \equiv 0$. Then, we analytically maximimize[8]

$$x^*_{q,\text{TC}} := \arg\max_{\bar{x}_q} \bar{x}_q, \text{ subject to } \|u\| \leq V_{\text{lim}},$$

and substitute it into (11) to find the desired u_{TC}. In order to visualize the effect of these controllers, we reparameterize u in terms of its polar angle $\phi := \angle u$ (note that the magnitude of u is effectively constrained by V_{lim} in each case).

Fig. 2 shows the contours of $\bar{x}_q$ according to (13) with $\bar{u} := V_{\text{lim}}(\cos\bar{\phi}, \sin\bar{\phi})$. We have shaded the region where $\bar{x}_q > V_{\text{lim}}/R$ (the "naive"[9] peak current). We also plot the ϕ chosen by the two conventional controllers (7), (8) compared to the task-specific controller (10). While the three controllers perform the same at stall, AC produces the highest torque at higher $|\omega_m|$, for both positive (when $\omega_m > 0$) and negative (when $\omega_m < 0$) work.

Despite the rather particular (and different) philosophical basis for the definition (10) (as opposed to the "x^*-seeking" motivation of (7), (8)), our observation here is that "unlocking" the second dimension of u in response to task specification affords benefits over the TA abstraction. Nonetheless, we investigate tracking and stability properties of (10) in more direct comparison to the conventional counterparts in III-B.

[7] taking the sign into account (for $\omega_m > 0$, the task entails positive work, and for $\omega_m < 0$, negative work)

[8] Using `Maximize[]` in Mathematica

[9] Compared to a scalar motor model, e.g. [1, eq. (1)].

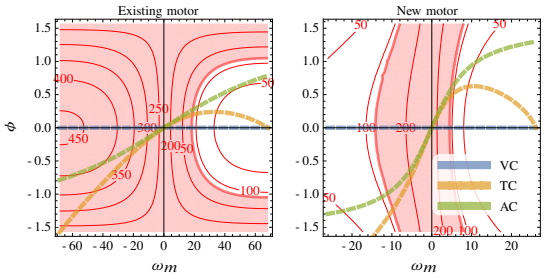

Figure 4: *Joule heating* $Rx^T x$ *in W:* dq-control revealing contours of power dissipated as heat, and also a comparison of 3 control strategies where they are trying to achieve max x_q. In the third quadrant where AC power output is particularly advantaged relative to TC, (averaged over speed) is only about 14% worse for the conventional motor and only about 20% worse for the hypothetical new design.

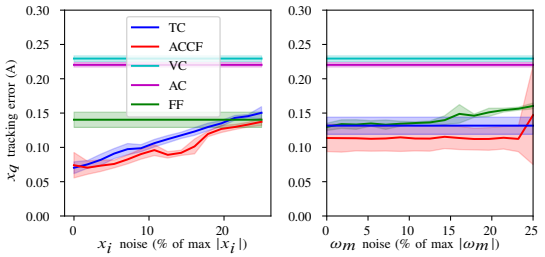

Figure 5: Empirical x_q-tracking performance of the controllers discussed in this paper—TC (7), VC (8), AC without and with current feedback (labeled "ACCF") for v (10), and FF (only the feedforward terms of (14))—when noise is injected into current (**left**) and speed (**right**) measurements. The horizontal axis shows the ratio of the standard deviation of the added noise to the maximum measurement experienced in these trials. The new ACCF strategy shows comparable or better tracking performance to the conventional TC controller, likely since it only needs feedback of x_q and not of x_d. The shaded regions show 1 standard deviation around the mean. The larger error at $\omega_m = 25$ rad/s using the ACCF is due to an outlier caused by power-supply limiting that was not accompanied by any systematic instability.

2) Peak power: The produced mechanical power (6) is $\tau_m \omega_m = k_e x_q \omega_m$, and so the same $u_\star$ is picked for each controller as in III-A1. Fig. 3 shows a similar plot, and this time the shaded region highlights regions where the produced power is larger than the naive peak power[10]

3) Efficiency in the presense of sensory noise: Fig. 5 shows the empirical performance of the conventional control strategies of Sec. II-B as well as the task-based strategy of Sec. III in the presence of noise.

The benefits of (10) compared to the conventional strategies comes at the expense[11] of Joule heating. Fig. 4 shows contours of the power dissipated as heat while using the same controllers as in III-A1–III-A2.

[10] Attained at half the no-load speed with a scalar model with $\omega_m = V/(2k_e)$ and $\tau_m/k_e = V_{\text{lim}}/(2R)$.

[11] However, as shown in Fig. 5, reliance on noisy sensory information can cause inefficiency as well. The "AC with current feedback" strategy still only relies on x_q-measurements only, unlike TC (7), which needs both components.

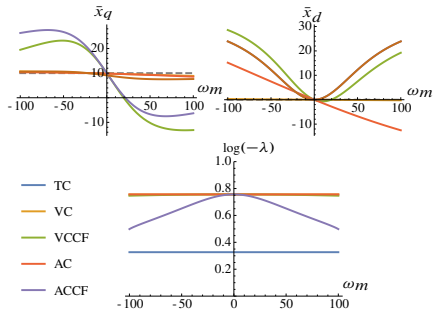

Figure 6: **Top:** Locus of $\bar{x}$-equilbria with the different strategies as ω_m is varied: TC (7) without the feedforward terms (with feedforward terms, $\bar{x} \equiv x^*$); VC (8) without and with current feedback, AC (10) without and with current feedback. **Bottom:** $\log_{10}(-\text{Re}(\lambda))$, where λ is the eigenvalue with the largest real part.

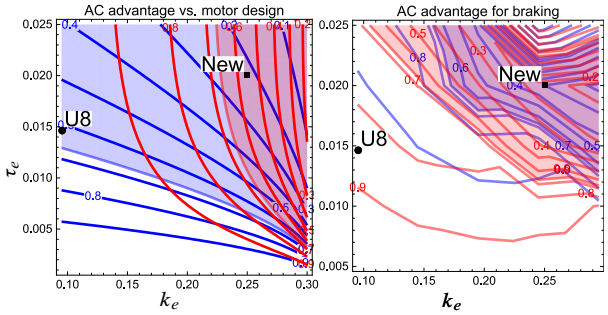

Figure 7: **Left:** The plot shows contours of the ratio of the peak τ_m produced using VC ((8), blue) and TC ((10), red) to the torque produced using angle control for peak torque (10). The axes vary the motor's electrical design parameters—the flux linkage k_e and electrical time constant τ_e—and the ratio is smaller than 2/3 where shaded. **Right:** Average torque over a braking task (numerical), where we can improve much more. The parameter values for the U8 are $(k_e, \tau_e) = (0.095, 0.014)$ in V/(rad/s), and seconds, and for a hypothetical "new motor," $(0.25, 0.02)$.

B. Tracking and Stability

After the equilibrium analysis III-A, now we investigate the properties of the linearization at these equilibria with the different strategies.

In Fig. 6, we first show the locus of an equilibrium $\bar{x}$ (12), as a function of ω_m. The first observation is that the coupling disturbances introduced through ω_m in (4) cause a large discrepancy in $|\bar{x}_q - x_q^*|$ at higher rotor speeds for VC (8) and AC (10) without current feedback. Fig. 6 also shows that introducing current feedback (the conventional method of compensating for the ω_m-coupling) is effective, but also invites the introduction of feedforward compensation using measurements of ω_m,

$$\widetilde{u}_{\text{AC}} = u_{\text{AC}} + k_e \omega_m e_1 - LA(\omega_m)x^*. \tag{14}$$

The bottom row of Fig. 6 shows that the equilibria (even if inaccurate) are stable with each controller. The plot shows the locus of the most unstable (largest real part) eigenvalue in a log scale, as a function of ω_m.

C. Relation to Motor Design

Fig. 7 shows a plot whose axes now correspond to motor design parameters, and the displayed quantity is the produced torque by the conventional control strategies as compared to (10), $\tau_{\text{VC}}/\tau_{\text{AC}}$ (blue) and $\tau_{\text{TC}}/\tau_{\text{AC}}$ (red). The contours show the level curves of these ratios, and the shaded regions correspond to where these ratios are $< 2/3$ (i.e. the conventional strategy produces less than 2/3 the torque of (10)).

Fig. 2–4 each show the performance curves of the hypothetical new motor (whose parameters are located on this plot) on their right panel. In order to ensure that our selected parameters are physically reasonable, we scale the resistance of the new motor in order to keep the same motor constant using its definition $K_m = k_e/\sqrt{R}$. The scaling of τ_e then must necessarily occur through an increase in L and/or n, neither of which present a fundamental obstruction. We present a sweep of motor catalog data in Sec. V.

The plot reveals that high k_e and high τ_e result in an amplification of the benefits of (10). Note that both of these parameters are related to the electrical properties of the motor (importantly, not winding-invariant). We discuss the trends of these parameters and others with various scale parameters in Sec. V. These results motivate further research into optimization of these non-conventional motor parameters at design-time, corresponding to usage of non-conventional strategies for control (10).

IV. dq-Control of Constrained Robotic Tasks

Next, we build on the findings of Sec. III and implement the new control strategies on a physical motor controller to test their effectiveness in robotic tasks. We use a Ghost Robotics U8 actuator module [11] with customized firmware.

Our test setup consists of a single actuator connected to a pulley, and a mass suspended from the pulley. This provides an approximately constant[12] external torque in (4), $\tau_{\text{ext}} \equiv mg\rho_p$, where ρ_p is the radius of the pulley.

While Sec. IV-A showcases the peak power output improvements of (10) in the real-world, IV-B shows that the "price to pay" in efficiency for this performance is negligible, suggesting that (10) is suitable for use in many robotics tasks, while providing greater performance in power-limited settings such as braking and leaping.

A. Braking

For these tests, we initially set the actuator to apply $\tau_m = 0$ and drop the mass. Following a velocity trigger ($\omega_m > \Omega$), the actuator is commanded with a constant voltage vector,

$$u_{\text{brake}}(u_d) = \text{constrain}(-V_{\text{lim}}, u_d), \tag{15}$$

and in different trials (shown in Fig. 8) we vary the parameter u_d. Note that when $u_d \neq 0$, the magnitude of the q-axis voltage is reduced so that $\|u\| = V_{\text{lim}}$. to exert the highest possible $u_q = -V_{\text{lim}}$, with a specified u_d, with the norm constrained to V_{lim} after. Note that $u_d = 0$ corresponds to the VC strategy (8).

Fig. 8 shows that spending the available voltage on the d-axis can provide an approximately 20% benefit to stopping

[12]The only caveat is that the cable must be kept under tension; in the hopping trials we limited the desired hopping height z^*, and applied a small upward force of $< 10\%$ the weight of the mass in the "aerial" phase.

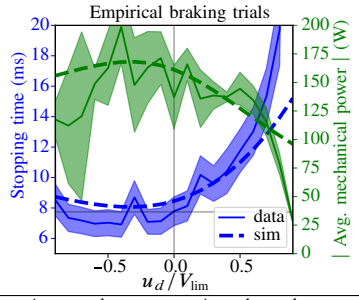

	Avg. mech. power	Avg. thermal power	Δt
TC	-143	106	3.86
ACCF	-153	113	1.99
AC	-229	218	0.58

Figure 8: **Top:** Usage of d-axis control in a braking task (Fig. 1) with fixed constant input voltage $u_{\text{brake}}(u_d)$ (15) reveals a benefit to stopping time as well as mechanical power output with nonzero u_d. **Bottom:** Metrics for the first half of the braking task (going from the trigger velocity Ω to $\Omega/2$) averaged over 3 trials show that AC achieves 60% greater power in 84% smaller time while doubling the thermal cost, while ACCF incurs only 6% greater thermal cost to give 7% greater power and 44% smaller time. We posit that the empirical performance deviates further from the simulation toward the u_d / V_{lim}-extremeties due to power-supply current-limiting, and inaccuracies in our knowledge of the parameters of (4).

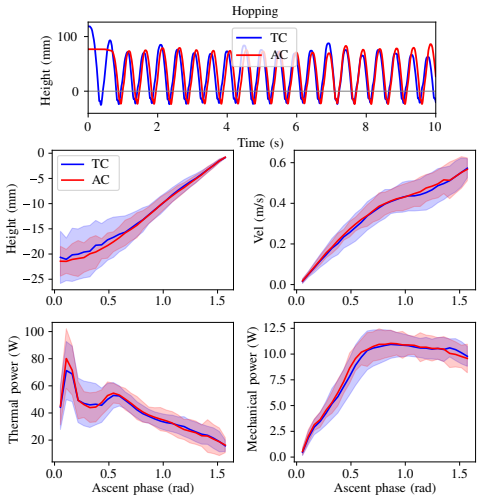

Figure 9: **Top:** Snippet of inverted hopping (Fig. 1) trials with the current-fed-back versions of TC (7) and AC (10). **Bottom:** The time average (1 standard deviation shaded) of the ascent states plotted against phase (17) over many hops reveals very similar qualitative behavior with the two controllers, as well as similar efficiency when recruited for this control task.

time as well as mechanical power output with the existing U8 motor (Fig. 1). In Fig. 7, we show that this benefit can be greatly amplified with different motor designs. In addition, we also apply the TC (7), AC, and ACCF (10) strategies empirically, with the results shown in the table.

Additionally, using numerical simulation of (4), we effectively validate the physical correspondence of our modeling and simulation by comparing it to the physical motor in the trials of Fig. 8.

B. Inverted 1DOF Hopping

The hardware setup of Fig. 1 allows for a fully instrumented vertical hopper implementation with a single actuator. We use the following hybrid controller

$$\tau_m = \begin{cases} 0, & \text{Aerial: } z > z_0 \\ \omega_{\text{hop}}^2 (z_0 - z), & \text{Descent: } z < z_0, \dot{z} < 0, \\ k_v(\sqrt{2gz^*} - \dot{z}), & \text{Ascent: } z < z_0, \dot{z} > 0. \end{cases} \quad (16)$$

This controller attempts to control the liftoff velocity (active damping control [22]) in the "ascent" phase, in order to control the hopping height. In order to compare control strategies, we change the controller u in (4) in the ascent phase, but employ the TC (7) in both aerial and descent phases. Fig. 9 shows time series plots of z the height of the mass using TC (7) and "AC with current feedback" (10) controllers, as well as mean and standard error from several variables plotted against vertical hopper phase [5] defined as

$$\psi_{\text{hop}} := \angle(-z\omega_{\text{hop}}, \dot{z}). \quad (17)$$

Both behaviors are stable and the qualitative performance is very similar (especially as seen in the lower rows of Fig. 9). In particular, despite the thermal downside of the AC controller (in peak torque operation) shown in Fig. 4, in a "real-world" control task, the Joule heating is comparable to the TC controller (lower left of Fig. 9). Thus, despite the new controller (10) being developed with the goal of maximizing peak torque output, it can be used for control tasks just as well as the conventional controller.

V. Motor Performance Scaling Relationships

Fundamental electromagnetic actuation performance limits have been extensively studied in the robotics literature using the winding-invariant K_m and its mass- and temperature-specific versions as a metric [1], [3]–[5], and measuring its empirical dependence on bulk mechanical parameters such as r_g, l, d (see Fig. 1, Table I).

However, Sec. III-C showed that even if K_m is fixed, operating in a different winding-dependent-parameter (k_e, τ_e) region than the existing motor[13] allowed for an amplification in peak torque and power density. Winding-dependent properties are far more sensitive to choices made by the motor manufacturer (potentially not published since it constitutes their intellectual property). This sensitivity and variability makes it more challenging to develop predictive models for these properties. In this paper we only vary n_t, a very small subset of the number of winding parameters available at the manufacturers' disposal.

Taking a cue from past work [1], [3], we develop tractable "scaling" models of relative performance (vs. other known motors) to explore the design space, and validate them against extensive motor catalog data. Though scaling models for K_m exist in prior work [1, Fig. 1], [3, Fig. 3, 5], we make some new contributions in the following ways: (a) we introduce a consistent set of assumptions on motor construction to analytically develop the scaling model (Assumption 1); (b) prior work has prioritized relating several performance metrics to a small subset of construction parameters—such as mass, or r_g—for model simplicity, but we instead prioritize a more

[13] which was selected by optimizing for thermal-specific K_m [4].

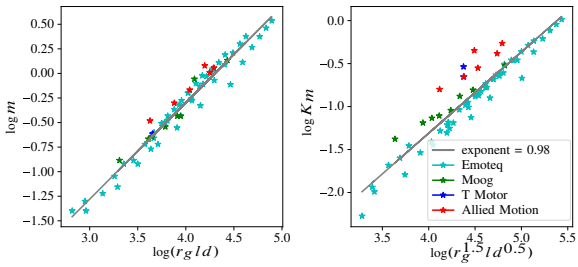

Figure 10: Scaling winding-invariant parameters mass and K_m, as compared to the scaling model (21) (which predicts that the slope in log-log scale should be 1) for a variety of motors from different manufacturers. Compared to prior work [3, Fig. 5], we see that a still "tighter" prediction of K_m as well as m can be obtained by incorporating all the stator dimensions (trading off model accuracy for complexity).

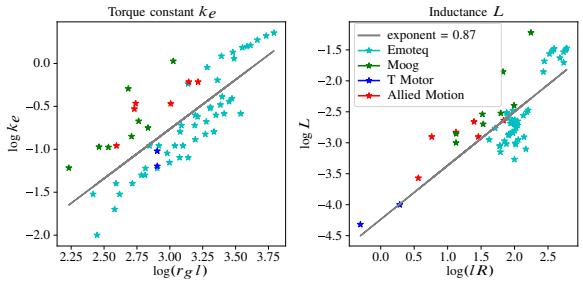

Figure 11: Scaling of electrical parameters with respect to construction parameters, where the slope in log-log scale is predicted to be 1 by our models in Sec. V.

detailed, hence accurate model[14] (Fig. 10) using appropriate combinations of a greater number of parameters (20), (21); (c) we propose and validate scaling relationships for winding-dependent parameters such as k_e, R, L (Fig. 11).

Assumption 1 (Motor construction)**.** *In reference to the physical parameters in Fig. 1, Table I, we assert that*

a) the volume of wire between adjacent stator teeth is small, i.e. $v_w \propto 2\pi r_g d$*;*[15]

b) we have a large gap-diameter motor for torque-demanding applications [3], expressed quantitatively in the parameter space by asserting $2\pi r_g \gg l$*;*

c) the motor mass is mostly due to the stator mass[16]*, and the stator mass is in turn proportional to the stator volume*[17]*, i.e.* $m \propto v_w = r_g d l$*.*

A. Detailed Scaling Model for K_m and K_m/m

First we develop a model for the torque produced on the permanent magnet rotor. The force per unit area on a loop of current-carrying wire (such as on a stator tooth) in a magnetic field of strength B is $\frac{\partial F}{\partial A} = iBn_t$, where i is the current [23].

The total area of all the stator teeth[18] is $\approx 2\pi r_g l$, and so the total shear force is $F \approx n_t i B l r_g 2\pi \implies \tau \approx 2\pi r_g^2 l n_t i B$. Using the usual defintion of the "torque constant" k_e in Nm/A, we divide τ above by i to get

$$k_e \approx 2\pi r_g^2 l n_t B, \tag{18}$$

Next, note that the resistance of the stator wire of length l_w and cross-section A_w is $R \propto l_w/A_w = l_w^2/v_w$, where v_w is the total volume of wire. From assumption 1*a)*, the total wire length is $l_w = 2(2\pi r_g + l)n_t$, and from assumption 1*b)* $l_w \approx 4\pi r_g n_t$. Putting these together,

$$\sqrt{R} \propto \frac{4\pi r_g n_t}{\sqrt{2\pi r_g d}}. \tag{19}$$

[14]Our justification for this added model complexity is that the added accuracy in the prediction of Fig. 10 is useful as a foundation for our models of the winding-dependent parameters.

[15]An alternate assumption–most of the wire located between the stator teeth—yielded poorer empirical fit than Fig. 10

[16]For instance, in the T-motor U8, the stator mass is 180g, and the rotor mass is 71g, or 28% of the motor mass.

[17]Justified since the stator volume is occupied by the ferrous core or copper wire, which have similar densities.

[18]Note that this is a more detailed model than $A_t \sim r_g$ in [3], which is important in our usage just before (22).

This depends on the independent parameters d, r_g, n_t, compared to the assumptions in [3] of $l_w \sim n_t l$ and $n_t \sim r_g$ which only consider the dependence of R on r_g, and ignore its relation to other scale parameters. The richer relation aids our arguments in the next subsection.

From (18), (19), we can calculate the winding-invariant

$$K_m = k_e/\sqrt{R} \sim r_g^{1.5} l d^{0.5}. \tag{20}$$

Using assumption 1*c)* together with the above, we get

$$K_m/m \sim (d/r)^{-0.5}, \tag{21}$$

i.e. the mass-specific K_m only depends on the aspect ratio of the annular stator. We validate this prediction across several motor catalogs in Fig. 10. The correspondence of our prediction to the catalog data provides some evidence to back our scaling relations, which we use to develop a scaling model for electrical parameters next.

B. Model for Winding-Dependent Characteristics

In the process of developing a scaling model for K_m, (18) shows how k_e depends on construction (r_g, l), material (B), and winding (n_t) parameters. The inductance of a single stator coil of area A_t (stator tooth) is $L_t = \frac{\mu_0 n_t^2 A_t}{d}$, [24, pg. 7.161] where μ_0 is the permeability of free space. As argued before, the total area of all the stator teeth is $A_t \sim r_g l$, and we can use (18) to replace n_t to get

$$L \sim \frac{n_t^2 A_t}{d} \sim Rl \implies \tau_e \sim L/R \sim l. \tag{22}$$

Fig. 11 shows scaling of both of these electrical parameters on motor catalog data.

We observe here that the mass-specific torque-production metrics $K_m/m, k_e/m$ are l-invariant (intuitively since increased l is equivalent to multiple motors being "stacked" in parallel [3]), and hence it does not affect selection criteria using those metrics [1], [3], [4]. However, (22) reveals its utility in setting the electrical properties of the motor relevant to its control (Sec. III-C).

C. "New Motor" Feasibility: Moving in (k_e, τ_e)-space

We can now predict the feasibility of the hypothetical motor of Fig. 7. First, we constrain the problem by fixing a desired m, i.e. from assumption 1*c)*,

$$r_g d l \sim 1 \implies \tau_e \overset{(22)}{\sim} l \sim r_g^{-1} d^{-1} \implies d \sim r_g^{-1} \tau_e, \tag{23}$$

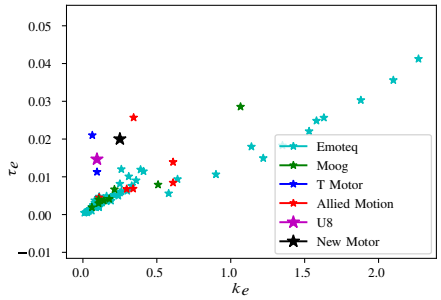

Figure 12: Catalog motors projected on the design plane of Fig. 7, with the new motor also superimposed. This shows that our existing U8 motor is already somewhat of an outlier in this parameter space (many of the T-motor motors are not plotted since their inductance data is not available).

as well as K_m, i.e. from (20)

$$1 \sim r_g^{1.5} l d^{0.5} \overset{\text{Assump. 1}c)}{\sim} (r_g/d)^{0.5} \overset{(23)}{\sim} r_g^2 \tau_e, \tag{24}$$

(assuming both are sized for the application by afore-cited conventional methods). From (18),

$$\begin{aligned} k_e &\sim r_g^2 l n_t \overset{(24)}{\sim} \tau_e^{-1} l n_t \\ k_e \tau_e &\sim l n_t. \end{aligned} \tag{25}$$

This relation obeys all the previous scaling relations, and thus suggests that we can create a motor with the same mass and K_m as an existing motor, and have remaining flexibility in both winding and construction parameters to move in the design space of Fig. 7. Fig. 12 shows the same parameter plane as Fig. 7, revealing that the majority of motors cut through a 1D slice of the k_e, τ_e design plane. We point out that unlike the argument just above which takes care to constrain K_m and m, the plot shows motors where those parameters vary due to sparsity of information at small regions of K_m, m-space. In the future, we plan to use FEMM software to more thoroughly investigate these design spaces.

VI. Conclusion and Future Work

In this paper, we have motivated research into moving past the TA abstraction of BLDC actuators and instead coupling its control and design to the tasks it is utilized for. In this initial paper, we have introduced a controller that demonstrates greater steady-state power output in analysis, numerical simulation, and real-world tasks. We have further shown that modifying conventional motor selection can amplify the benefit of the new controller, and suggested a hypothetical motor design that would do so based on scaling models. Future work will include on one hand exploring other new control strategies that reap benefits beyond the TA abstraction, such as external torque estimation, adaptive parameter estimation, maximizing efficiency, etc. On the other hand, we hope to perform numerical optimization of motor parameters for task-specific performance, and we hope to construct new motors based on our predictions and demonstrate drastic performance improvements compared to the current state-of-the art.

Acknowledgements

We thank the authors of [14] for sharing the Emoteq motor catalog, Ghost Robotics for enabling the implementation of custom motor control algorithms on commercial hardware, and the anonymous reviewers for helping improve the paper.

References

[1] J. M. Hollerbach, I. W. Hunter, and J. Ballantyne, "A comparative analysis of actuator technologies for robotics," *Robotics Review*, vol. 2, pp. 299–342, 1991.
[2] R. M. Murray, Z. Li, S. S. Sastry, and S. S. Sastry, *A mathematical introduction to robotic manipulation*. CRC press, 1994.
[3] S. Seok, A. Wang, D. Otten, and S. Kim, "Actuator design for high force proprioceptive control in fast legged locomotion," in *Intelligent Robots and Systems (IROS), 2012 IEEE/RSJ International Conference on*. IEEE, 2012, pp. 1970–1975.
[4] G. Kenneally, A. De, and D. E. Koditschek, "Design Principles for a Family of Direct-Drive Legged Robots," *IEEE Robotics and Automation Letters*, vol. 1, no. 2, pp. 900–907, July 2016.
[5] A. De, "Modular Hopping and Running via Parallel Composition," Ph.D. dissertation, University of Pennsylvania, 2017.
[6] K. Galloway, G. Haynes, B. D. Ilhan, A. Johnson, R. Knopf, G. Lynch, B. Plotnick, M. White, and D. Koditschek, "X-RHex: A Highly Mobile Hexapedal Robot for Sensorimotor Tasks," Tech. Rep., Nov. 2010.
[7] T. Miller, "Brushless permanent-magnet motor drives," *Power engineering journal.*, vol. 2, no. 1, pp. Power engineering journal. , 1988, Vol.2(1), p.55, 1988.
[8] J. R. Mevey, "Sensorless field oriented control of brushless permanent magnet synchronous motors," Ph.D. dissertation, Kansas State University, 2009.
[9] T. A. Lipo, *Vector control and dynamics of AC drives*. Oxford university press, 1996, vol. 41.
[10] "T-motor u8," 2018, http://store-en.tmotor.com/goods.php?id=322.
[11] "Ghost robotics," 2018, http://www.ghostrobotics.io/.
[12] H. Asada and K. Youcef-Toumi, *Direct-drive robots: theory and practice*. MIT press Cambridge, MA, 1987.
[13] B. Hannaford, P.-H. Marbot, P. Buttolo, M. Moreyra, and S. Venema, "Scaling of direct drive robot arms," *The International journal of robotics research*, vol. 15, no. 5, pp. 459–472, 1996.
[14] P. M. Wensing, A. Wang, S. Seok, D. Otten, J. Lang, and S. Kim, "Proprioceptive Actuator Design in the MIT Cheetah: Impact Mitigation and High-Bandwidth Physical Interaction for Dynamic Legged Robots," *IEEE Transactions on Robotics*, pp. 1–14, 2017.
[15] A. De, G. Lynch, A. Johnson, and D. Koditschek, "Motor sizing for legged robots using dynamic task specification," in *2011 IEEE Conference on Technologies for Practical Robot Applications (TePRA)*, Apr. 2011, pp. 64 –69.
[16] C. Hwang, P. Li, C. Liu, and C. Chen, "Design and analysis of a brushless DC motor for applications in robotics," *IET Electric Power Applications*, vol. 6, no. 7, p. 385, 2012.
[17] S. Ogasawara, M. Nishimura, H. Akagi, A. Nabae, and Y. Nakanishi, "A high performance AC servo system with permanent magnet synchronous motors," *IEEE Transactions on Industrial Electronics*, no. 1, pp. 87–91, 1986.
[18] D. Wilson, "Teaching your PI controller to behave," 2015.
[19] J. C. Gamazo-Real, E. Vázquez-Sánchez, and J. Gómez-Gil, "Position and speed control of brushless dc motors using sensorless techniques and application trends," *Sensors*, vol. 10, no. 7, pp. 6901–6947, 2010.
[20] M. Piccoli and M. Yim, "Anticogging: Torque ripple suppression, modeling, and parameter selection," *The International Journal of Robotics Research*, vol. 35, no. 1-3, pp. 148–160, Jan. 2016.
[21] S.-I. Park, T.-S. Kim, S.-C. Ahn, and D.-S. Hyun, "An improved current control method for torque improvement of high-speed BLDC motor," in *Applied Power Electronics Conference and Exposition, 2003. APEC'03. Eighteenth Annual IEEE*, vol. 1. IEEE, 2003, pp. 294–299.
[22] G. Secer and U. Saranli, "Control of monopedal running through tunable damping," in *2013 21st Signal Processing and Communications Applications Conference (SIU)*, Apr. 2013, pp. 1–4.
[23] S. Liao, P. Dourmashkin, and W. Belcher, *Introduction to Electricity and Magnetism: MIT 8.02 Course Notes*. Pearson Custom Pub.
[24] P. Wicksteed, *Physics*, ser. Loeb classical library. Heinemann, 1957, no. v. 1.